Journal of Micromechanics and Microengineering

PAPER

Optical imaging and image analysis for high aspect ratio NEMS

To cite this article: R R A Syms *et al* 2019 *J. Micromech. Microeng.* **29** 015003

View the article online for updates and enhancements.

IOP ebooks™

Bringing you innovative digital publishing with leading voices to create your essential collection of books in STEM research.

Start exploring the collection - download the first chapter of every title for free.

This content was downloaded from IP address 129.31.139.57 on 20/11/2018 at 13:17

IOP Publishing Journal of Micromechanics and Microengineering
J. Micromech. Microeng. **29** (2019) 015003 (11pp) https://doi.org/10.1088/1361-6439/aaecce

Optical imaging and image analysis for high aspect ratio NEMS

R R A Syms[1,3], A Bouchaala[1], O Sydoruk[1] and D Liu[2]

[1] EEE Department, Imperial College London, Exhibition Road, London, SW7 2AZ, United Kingdom
[2] Optical and Electrical Department, Changzhou Institute of Technology, 666 Liaohe Road, Changzhou, Jiangsu Province, People's Republic of China

E-mail: r.syms@imperial.ac.uk

Received 24 August 2018, revised 19 October 2018
Accepted for publication 30 October 2018
Published 20 November 2018

Abstract
A strategy for optical microscopy of high-aspect-ratio (HAR) nanoelectromechanical systems (NEMS) that combine large feature spacing and large height with sub-wavelength width is presented. Line images are simulated using a 2D model of incoherent imaging based on modal diffraction theory. Beyond a sufficient depth, it is shown that sub-wavelength features appear as dark lines, while wider features are visible as their edges. The results suggest NEMS and MEMS may be separated from background in images by detection of valleys in brightness. Results are confirmed by imaging of Si NEMS containing 100 nm wide features in a bright-field microscope. Algorithms for separation of NEMS, MEMS and background in microscope images based on valley detection, thresholding and masking are demonstrated.

Keywords: NEMS, MEMS, sub-wavelength imaging, image segmentation

(Some figures may appear in colour only in the online journal)

1. Introduction

Nanoelectromechanical systems (NEMS) are likely to impact on sensor technology, by virtue of their smaller size, reduced mass and larger surface-to-volume ratio [1, 2]. Conventionally, silicon NEMS are patterned by electron beam lithography, structured by plasma etching and visualized in a scanning electron microscope (SEM). However, the slow speed and high cost of serial direct-write patterning limits manufacturability. SEM inspection has a similarly limited throughput, and in addition may charge and heat suspended nanoscale parts. Although parallel patterning based on sidewall transfer lithography (STL) has been developed to form restricted device layouts [3–5], there is a need for correspondingly simple methods of device metrology. Out-of-plane displacements have been made by interferometry [6], but there are still difficulties in measuring in-plane features.

Here we again propose an optical approach, as counter-intuitive as it may sound. It is not obvious that NEMS may be seen at all in an optical microscope, or how they may appear. However, both aspects may be clarified using experiments and simple theoretical models. For example, sub-wavelength optical metrology has long been of interest in microelectronics, and it is well known that widely spaced features are visible in an optical microscope [7–9]. Methods of predicting one-dimensional (1D) line-shapes have been developed for thick and thin structures. Despite their flexibility, numerical simulation packages are less helpful, because of their lengthy run-times. Instead, isolated features are normally modelled as part of a periodic grating, and the problem of diffraction of an incident plane wave is solved exactly. Line images are then constructed by integrating the back-scattered field over the range of illumination wavelengths, illumination angles and collection angles allowed by the imaging system. Older methods use approximate diffraction theory [10, 11], while more recent methods (notably those of Nyyssonen [12, 13] and Sheridan [14–16]) use rigorous modal [17–19] or coupled mode [20, 21] theory. Due to the multiple integrals involved, calculations are still long. Few authors therefore consider white light or plane images [22, 23], and little attempt has been made to tackle the feature shapes and index contrast inherent in NEMS.

Knowing likely feature appearance, a suitable image processing strategy may be developed. Feature extraction has

[3] Author to whom any correspondence should be addressed.

 © 2018 IOP Publishing Ltd Printed in the UK

been developed for biological [24, 25] and medical [26] image analysis, character [27] and fingerprint [28] recognition, PCB inspection [29] and fault detection in integrated circuits [30]. Often the image is filtered to reduce noise [31]. Targeted techniques are then used to enhance specific features. Solid objects are detected by their edges [32], for example using the Sobel [33] or Canny [34] filters. Line features are detected as valleys in brightness [35, 36]. Statistical approaches are then used to partition the features into classes [37, 38], for example using the Otsu method [39, 40]. Post processing such as skeletonization [41] is then used for line sharpening before object recognition. However, there appears to have been no attempt to adapt such techniques to MEMS or NEMS metrology.

Here we attempt to develop a suitable strategy. Fabrication of NEMS by STL is briefly reviewed in section 2 and example structures for imaging are presented. Modeling of white-light imaging of MEMS and NEMS features is described in section 3. Line images of etched structures are simulated using a 2D model based on modal diffraction theory and is shown that widely-spaced NEMS features are indeed visible, but appear as dark lines on a bright background, while MEMS appear as outline edges. The development of suitable image processing algorithms is described in section 4. Here the difficulty is to partition the image into two valley features (MEMS and NEMS) and substrate background. The multilevel Otsu method is used for separation of valley and non-valley features and a new algorithm based on local masking is used to separate valley classes. Conclusions are drawn in section 5.

2. High-aspect-ratio (HAR) NEMS

HAR NEMS have been fabricated in bulk silicon and bonded silicon-on-insulator (BSOI), using optical and multi-layer STL followed by deep reactive ion etching (DRIE) and undercut. Briefly, the substrate is first patterned with resist, using polygonal features whose perimeters define a set of nanoscale parts with microscale separations. The pattern is then transferred into the substrate to a shallow depth by DRIE [42]. The resist is then stripped, and the mesas thus formed are coated with a thin semi-conformal layer of material. Horizontal layers are then removed to leave the vertical surfaces as a sidewall mask. For more complex devices, the cycle can be repeated to define a second set of nanoscale parts [4].

The substrate is then planarised with thick resist, which is patterned to define microscale features such as anchors and electrodes. The surface pattern is transferred into the substrate by DRIE to form MEMS and NEMS together. For bonded BSOI, etching can stop at the oxide interlayer, and movable parts freed by oxide removal [43]. For bulk Si, parts are undercut by isotropic plasma etching. After resist stripping, metallisation may be added for electrical contact. Figure 1(a) shows an example NEMS structure and figure 1(b) shows cross- sections along the lines A–A and B–B. The first mainly shows microscale features, but a shallow legacy mesa may be seen at the attachment point of nanoscale parts. The second shows microscale and suspended nanoscale features. Thus, optical images of three characteristic edge feature types are likely to be present in any microscope view.

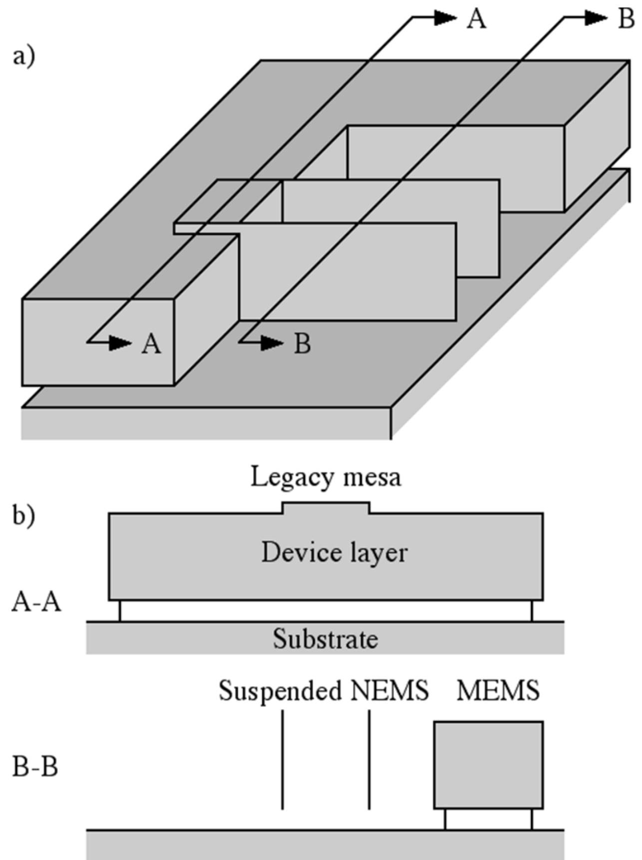

Figure 1. (a) Representative HAR NEMS device; (b) device cross-sections at A–A and B–B.

Figure 2 shows SEM views of test structures chosen to present different demands from image processing. In each case, all nanoscale parts consist of 100 nm wide features etched to a depth of 4 μm, and the minimum feature spacing is 10 μm. Figures 2(a) and (b) show examples fabricated in bulk Si (a spiral spring and a micro-gripper). Similarly, figures 2(c) and (d) show examples formed in BSOI (cellular materials with different lattices [5]). Devices in the left-hand figures have been defined using single layer STL. Those in the right-hand figures have required double layer STL, which removes many but not all of the layout constraints of single layer STL. The micro-gripper in figure 2(b) has an asymmetric tip, formed by assigning the grip to the MEMS layer on one side and to a STL NEMS layer on the other and hence creating intersecting nanoscale features. Resist used to define microscale parts has been left in place in figures 2(a) and (b), while sidewall material is present in all cases. Thus, legacy mesas may be seen clearly where nanoscale parts attach to microscale anchors in the lower figures, while these features are blurred in the upper figures. The aim of simulation is to anticipate the appearance of such features in an optical microscope.

3. Optical simulation

Figure 3(a) shows the simulation model, which contains a three-layer relief structure. Layer 1 is the surround (air) with relative dielectric constant $\varepsilon_{r1} = 1$. Layer 2 contains NEMS features (mesas with width w and depth d in a material with

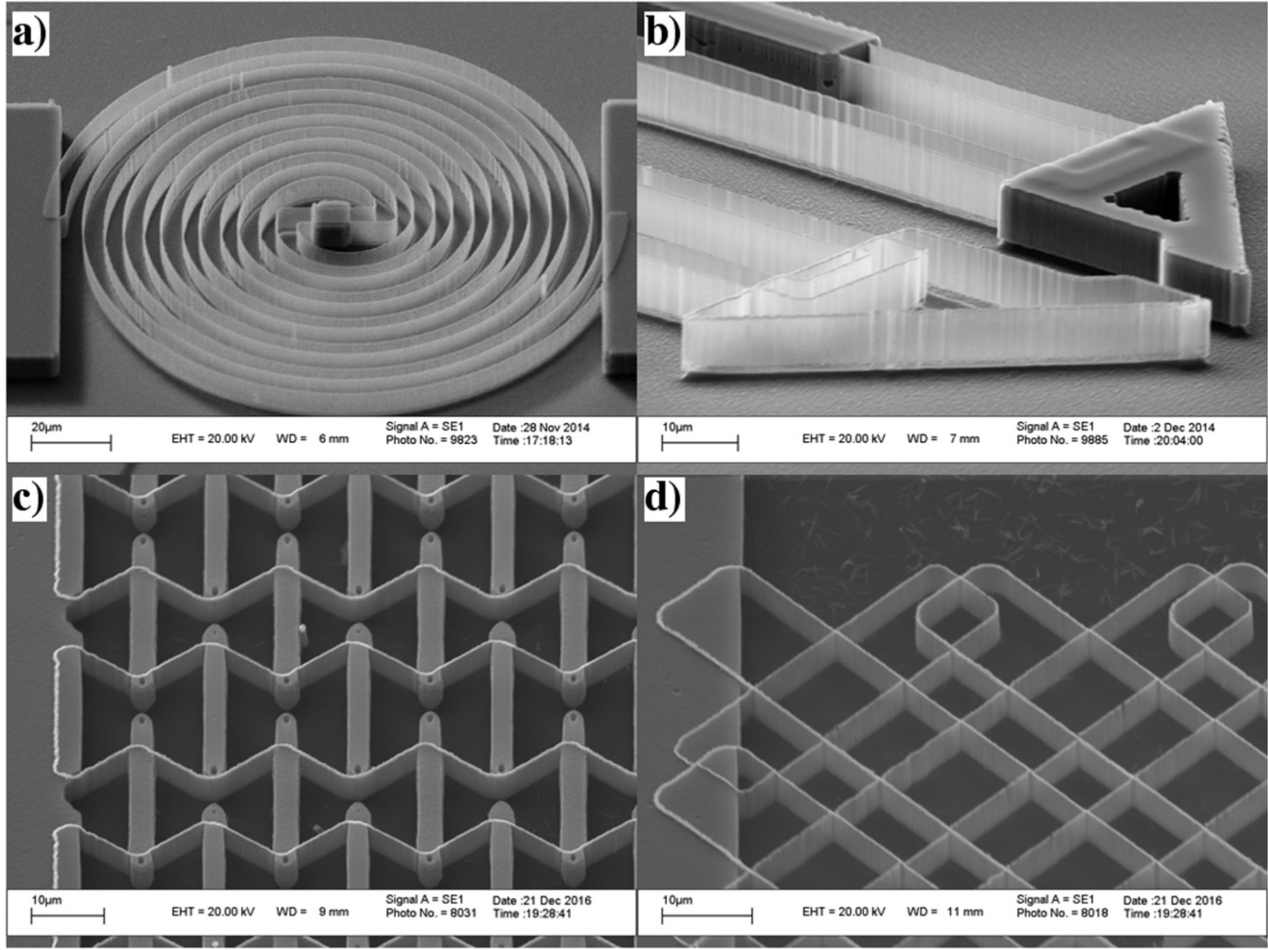

Figure 2. SEM photographs of HAR NEMS devices: (a) spring, (b) gripper; (c) and (d) 2D cellular materials with different lattices. Devices (a) and (b) have photoresist remaining.

relative permittivity ε_{r2a}) surrounded by air ($\varepsilon_{r2b} = \varepsilon_{r1}$). For intrinsic Si at wavelengths near 0.5 μm (green light) we assume $\varepsilon_{r2a} = 11.7–j\ 0.272$ [44, 45]. Layer 3 is the substrate, which has relative permittivity ε_{r3}, here taken as ε_{r2a}. The structure has period Λ as shown in figure 3(b), and the permittivity distribution $\varepsilon_{r2}(z)$ is written as:

$$\varepsilon_{r2}(z) = \sum\nolimits_{I} \sigma_I \varepsilon_{r2I} \cos(I2\pi x/\Lambda). \tag{1}$$

Here the summation is from $I = 0$ to I_{max}, the maximum number of terms considered, and $\varepsilon_{r2I} = (2/I\pi)\ (\varepsilon_{r2a} - \varepsilon_{r2b})\ \sin(I\pi w/\Lambda)$. The term σ_I is the Lanczos sigma function $\mathrm{sinc}\{I\pi/(I_{max}+1)\}$, which is used to reduce ringing at discontinuities in permittivity.

For TE incidence we may write the electric field in the ith layer as $E_i = E_{yi}(x, z)\ j$. At wavelength λ, the problem is then to solve the scalar wave equations:

$$\nabla^2 E_{yi} + \varepsilon_{ri} k_0^2 E_{yi} = 0. \tag{2}$$

Where $k_0 = 2\pi/\lambda$. For plane wave incidence at an angle θ, the field in Layer 1 may be taken as the sum of the incident wave and a set of reflected diffraction orders, as shown in figure 3(c):

$$\begin{aligned} E_{y1} &= \exp\{+jk_x(x-d)\}\exp(-jk_z z) \\ &\quad + \sum_L r_L \exp\{-jk_{x1L}(x-d)\}\exp(-jk_{zL}z). \end{aligned} \tag{3}$$

Here $k_x = k_1\cos(\theta)$ and $k_z = k_1\sin(\theta)$ are the x- and z-components of the propagation constant of the incident wave, with $k_1 = k_0\sqrt{\varepsilon_{r1}}$. Similarly, r_L is the amplitude of the Lth order, $k_{zL} = k_z + LK$ is the z-component of its propagation constant, $K = 2\pi/\Lambda$, and the summation is from $-L_{max}$ to $+L_{max}$, where L_{max} is the number of orders considered. Substitution into the wave equation for Layer 1 yields $k_{x1L} = \sqrt{(\varepsilon_{r1}k_0^2 - k_{zL}^2)}$. k_{x1L} will be imaginary once $k_{zL}^2 > \varepsilon_{r1}k_0^2$, so the diffraction orders will be evanescent for sufficiently large $|L|$.

Similarly, the field in Medium 3 is a set of transmitted diffraction orders:

$$E_{y3} = \sum_L t_L \exp(+jk_{x3L}x)\exp(-jk_{zL}z). \tag{4}$$

Here t_L is the amplitude of the Lth transmitted order. Substitution into the wave equation for Layer 3 gives $k_{x3L} = \sqrt{(\varepsilon_{r3}k_0^2 - k_{zL}^2)}$. However, because layer 2 is non-uniform, the solution here must be assumed as a sum of eigenmodes, namely:

$$E_{y2} = \sum_{\nu} \left\{ [A_{\nu} \exp(+jk_{x2\nu}x) + B_{\nu} \exp(-jk_{x2\nu}x)] \right.$$
$$\left. \sum_{L} a_{L\nu} \exp(-jk_{zL}z) \right\}. \quad (5)$$

Here ν is the mode number, $k_{x2\nu}$ is the propagation constant of the νth mode, A_{ν} and B_{ν} are the amplitudes of the νth forward and backward going modes, and the terms $a_{L\nu}$ $\exp(-jk_{zL}z)$ (when collected together for a particular value of ν) define mode shapes that must be found. The notation again implies a summation range determined by the number ν_{max} of modes retained.

Substituting into the wave equation for Layer 2 we obtain $-(k_{x2\nu}^2 + k_{zL}^2)\ a_{L\nu} + k_0^2\Sigma_I\ \varepsilon_{r2I}\ a_{L+I\nu} = 0$. These equations can be written in the form $(M - k_{x2\nu}^2 I)\ a_{\nu} = 0$. Here I is the identity matrix, M is a square matrix with elements $M(L, L) = -k_{zL}^2 + k_0^2\varepsilon_{r20}$; $M(L, L+I) = k_0^2\varepsilon_{r2I}$ for $I \neq 0$, and a_{ν} is the column vector $(a_{-L\max\nu} \ldots a_{-1\nu}, a_{0\nu}, a_{1\nu}, \ldots a_{L\max\nu})^T$. The equations can be solved for $k_{x2\nu}$ and a_{ν}, and the overall solution found by matching at boundaries. For TE incidence this involves matching E_y and $\partial E_y/\partial x$ at $x = 0$ and $x = d$; the result is a matrix equation for the unknowns r_L, t_L, A_{ν} and B_{ν}.

Once the expansion coefficients are known, the complete field may be reconstructed. For example, figure 4(a) shows the variation of $|E|$ on the (z, x) plane, assuming TE incidence at $\theta = 0$, $\lambda = 0.5\ \mu$m on a Si feature of width 0.1 μm and depth 4 μm, with $\Lambda = 10\ \mu$m. The field pattern is symmetric, and results from a combination of diffraction, reflection from horizontal Si surfaces and interference. A similar procedure may be used for TM incidence, solving the wave equation for H_y; the electric field components E_x and E_z may then be found from the Maxwell curl relation. Figure 4(b) shows the variation of $|E|$, assuming TM incidence at $\theta = 20°$. The overall pattern is now highly asymmetric, due to the additional effects of reflection from vertical Si surfaces and shadowing. We have obtained near-identical results with the commercial multi-physics simulation package COMSOL®, albeit through a much longer calculation.

Imaging is then modeled as shown in the remainder of figure 3(a), which shows a lens with numerical aperture NA = $\sin(\theta_{max})$ arranged for unity magnification. White-light illumination is simulated by assuming plane wave incidence at a discrete set of N_{λ} wavelengths λ and a set of N_{θ} angles θ, limited by the angle θ_{max} and weighted by aplanatic factors $\cos^{1/2}(\theta)$ [15]. Each wave generates a back-scattered field, described by the summation in (3) and consisting of a fan of diffraction orders. Of those that are propagating, only the set whose angles θ_L lie within the acceptance cone of the lens can contribute to the image, again weighted by aplanatic factors.

It is simple to select and weight orders from the back-scattered field at the object plane ($x = d$) to form a line image at the image plane, with contributions from each wavelength, angle and polarization being summed incoherently. However, the need to retain sufficient terms in the expansion of ε_{r2} together with sufficient diffraction orders and modes makes the calculations lengthy, and convergence must be

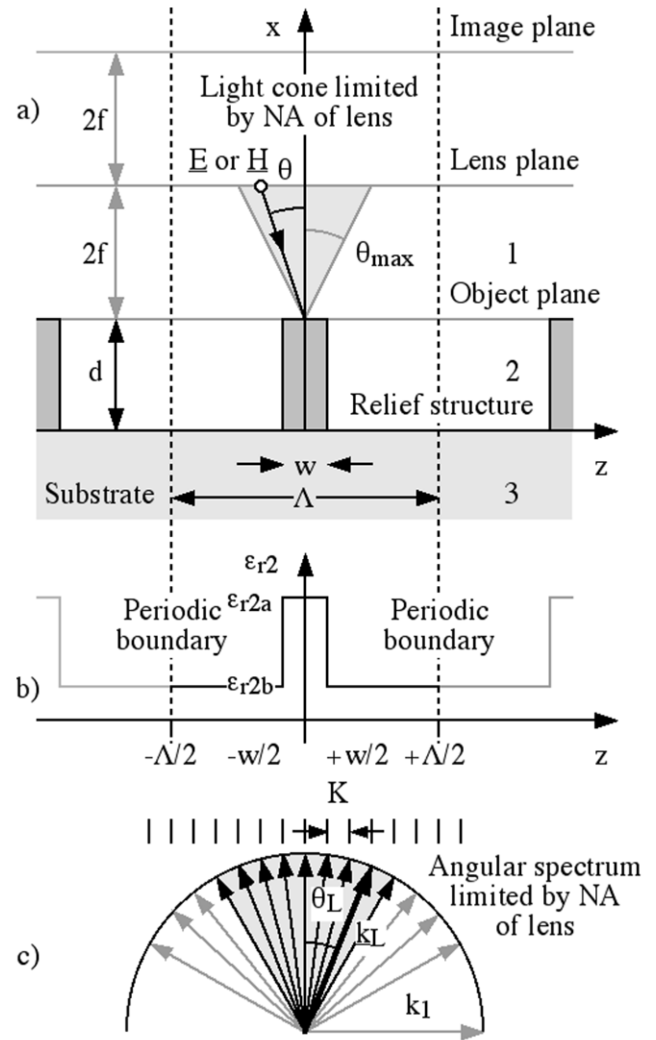

Figure 3. Simplified model of optical imaging: (a) overall system, (b) assumed permittivity variation and (c) effect of lens on angular spectrum of diffracted waves.

carefully checked. We have assumed $I_{max} = \nu_{max} = L_{max}$, with $L_{max} = 240$ throughout.

Figures 5(a) and (b) shows 1D field variations calculated from the 2D variations in figures 4(a) and (b). In each case, the black line shows the total back-scattered field on $x = 0$ (the 'object'), while the grey line shows the field after rejection of evanescent waves and diffraction orders outside a cone of half-angle $\theta_{max} = 30°$ (the 'image'). The effect of the lens is to remove high spatial frequencies [10]. Once again, we have verified these results with COMSOL®, using the less accurate approach of discrete Fourier transformation and low-pass filtering to simulate the effect of the lens.

Unfortunately, the results are sensitive to calculation details (especially feature depth), because the modes of Layer 2 are effectively resonant in a low-Q cavity between the substrate and air. There is little improvement if a range of illumination angles is included, since the effects are coherent. Despite this, oscillations are reduced if the feature depth is greater than around 2λ and a range of wavelengths is included. Under these circumstances, illumination is incoherent, etalon effects average out, and the normal experience of microscopy is restored.

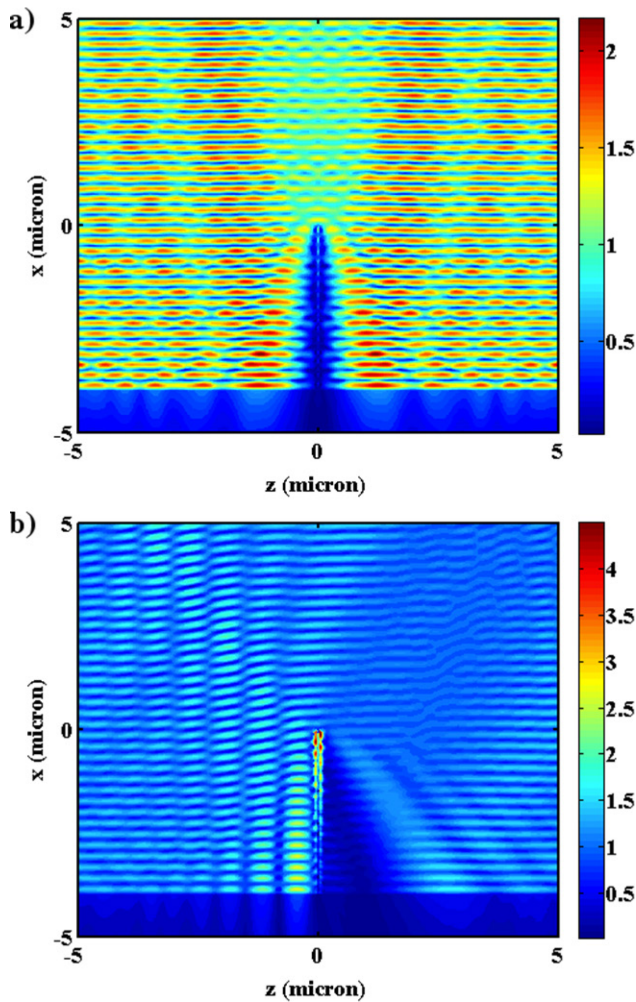

Figure 4. Numerical calculation of 2D fields near nanoscale feature at 500 nm wavelength: (a) TE polarization, at $\theta = 0°$; (b) TM polarization at $\theta = 20°$.

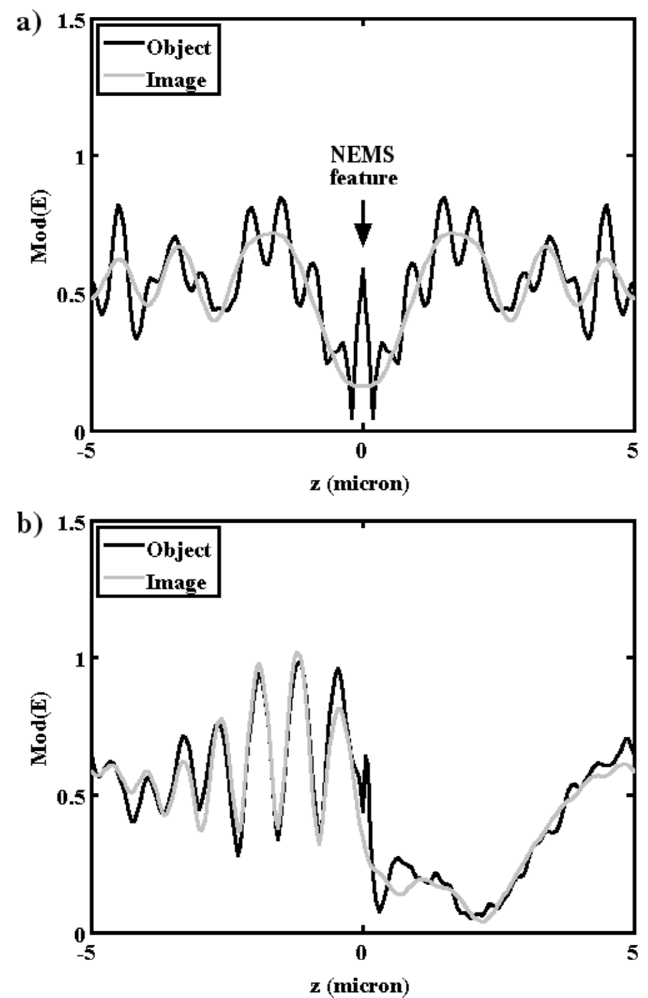

Figure 5. Numerical calculation of 1D fields at 500 nm wavelength: (a) TE polarization, at $\theta = 0°$; (b) TM polarization at $\theta = 20°$. Different lines show line object and image.

Figure 6(a) shows line images of a feature with $w = 0.1$ μm, $d = 4$ μm and $\Lambda = 10$ μm, obtained by assuming $N_\lambda = 21$ wavelengths in the range 400–700 nm and $N_\theta = 21$ angles in the range $-\theta_{max}$ to θ_{max}. For simplicity we assume that substrate properties and illumination are independent of λ and restrict ourselves to TE polarization. Results are shown for three values of θ_{max} (10°, 20° and 30°, or NA = 0.17, 0.34, and 0.5). Variations are plotted as power, normalised to the peak.

In each case, the result is similar: the sub-wavelength Si feature is visible as a reduction in intensity, with the sharpness increasing as NA rises. The explanation is scattering by the nanostructure, which locally diverts power into diffraction orders lying outside the acceptance cone of the lens. The reduction increases rapidly as the feature height increases from zero, and then gradually reduces to stabilise at the value shown, implying that even shallow features will be visible. Figure 6(b) shows results for a much wider feature, with $w = 2$ μm. Here, the reduction in intensity is smaller, and takes place at feature edges. Unfortunately, it has been impossible to verify these incoherent imaging results using COMSOL®, due to the calculation time required.

Similar results are obtained with other silicon feature dimensions. For example, figure 7(a) shows the variation of the TE line image minimum with feature depth d, for $w = 0.1$ μm, $\Lambda = 10$ μm and three different values of θ_{max} (10°, 20° and 30°). For small d, the results are close to unity, implying little scattering. As d rises, they fall, while oscillating at a rate consistent with coherent addition of reflections from mesa and substrate. The oscillations die away when the reflections add incoherently, and all three traces tend to a similar value at large d. However, more rapid convergence is achieved as θ_{max} rises, reinforcing the benefits of lenses with larger NA. For wider features (say, $w = 2.0$ μm), similar results are obtained, but with higher limiting values of the minima, as previously shown in figure 6(b).

Figure 7(b) shows variations with feature width w, at a constant depth $d = 4$ μm, for the same three lenses. The results are again close to unity at very small w, falling rapidly as w rises. In the NEMS region (between $w \approx 20$ nm and $w \approx 100$ nm), minima are therefore low. In the MEMS region (for $w > 0.4$ μm at the highest NA shown), they tend to a higher value. The transition is again regulated by the value of θ_{max}, and the differences are responsible for the contrast

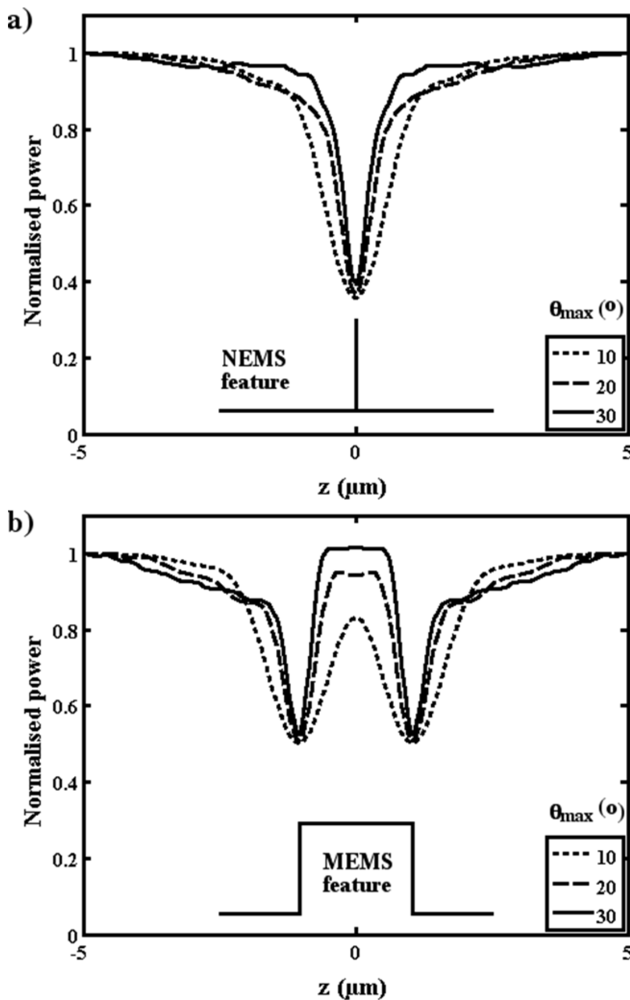

Figure 6. Simulated line images of Si features with 4 μm depth and (a) 0.1 μm and (b) 2 μm width, calculated assuming TE polarization, white light illumination between 400 nm and 700 nm wavelength, and lenses with $\theta_{max} = 10°$, 20° and 30°.

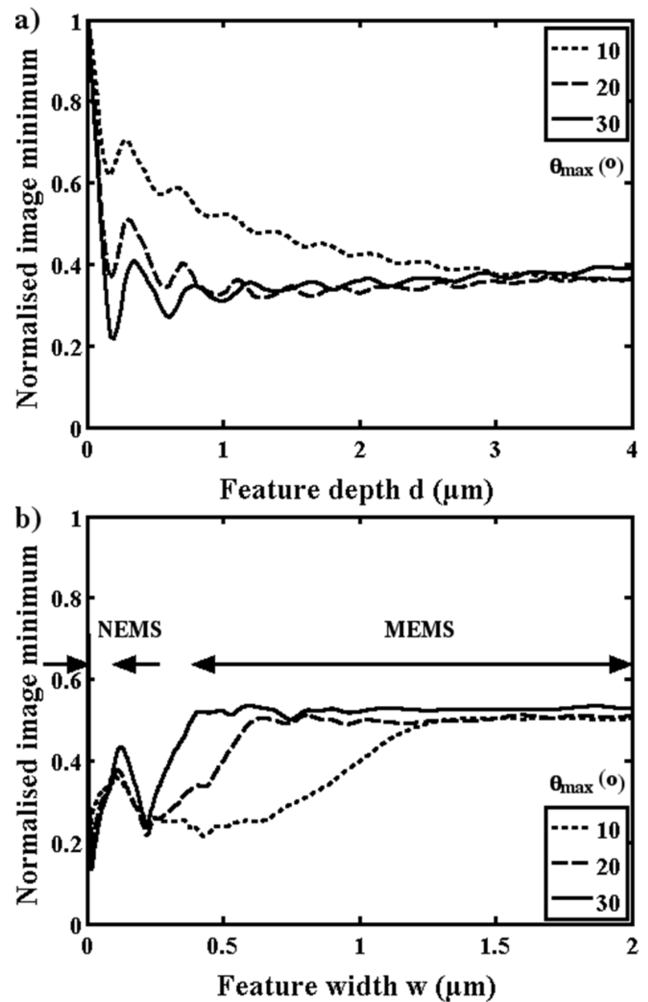

Figure 7. Variations in line image minima (a) with feature depth, at constant width $w = 0.1$ μm, and (b) with feature width, at constant depth $d = 4$ μm, for lenses with $\theta_{max} = 10°$, 20° and 30°.

investigated here. In between, there are additional peaks and troughs that appear to be associated with excitation of in-plane resonances. These aspects require further investigation, but we have found that qualitatively similar results are obtained for different periods Λ, depths d, and permittivities $\mathrm{Re}(\varepsilon_{r2a})$. Thus, although the contrast mechanism may not be universal, there is a strong likelihood that NEMS and MEMS may generally be differentiated.

4. Optical imaging and image processing

The simulations show that widely spaced NEMS features and the edges of MEMS should appear as valleys in image brightness, with the former being deeper. However, a lens with high NA is needed to maximise resolution. Other diffraction effects will cause additional variations in apparent substrate brightness, as will surface debris. Less importantly, non-uniform illumination will cause variations in local brightness; this can be mitigated using local thresholding, but should be unimportant with Kohler illumination. Edge effects can arise in video cameras; these must be cropped, since they otherwise introduce a spurious feature class.

Imaging was carried out using a Leica DMR white light microscope using ×5, ×20 and ×50 objectives (NA = 0.15, 0.40 and 0.55). The best results were obtained with ×50 objective. Black and white images with 640 × 480 pixels were acquired in using a Donpisha 3CCD camera module and Debut Video Capture software. Image processing was performed in MATLAB. Figure 8(a) shows an image of half of the spring feature in figure 2(a). Here the resist-coated microscale anchor may be seen as a darker area on the left and the substrate as a light area on the right. As predicted, the nanoscale spring is visible as a set of dark lines, and its attachment to the legacy mesa may also be seen. The substrate is generally bright, but its appearance varies slightly between the nanoscale features.

It should be possible to separate NEMS, MEMS and substrate background into different classes. Obvious criteria are image brightness and valleys in brightness; however, there may be others. The brightness B on the (y, z) plane is available directly. Figure 8(b) shows the histogram of B, which mainly presents the bimodal distribution of the anchor and

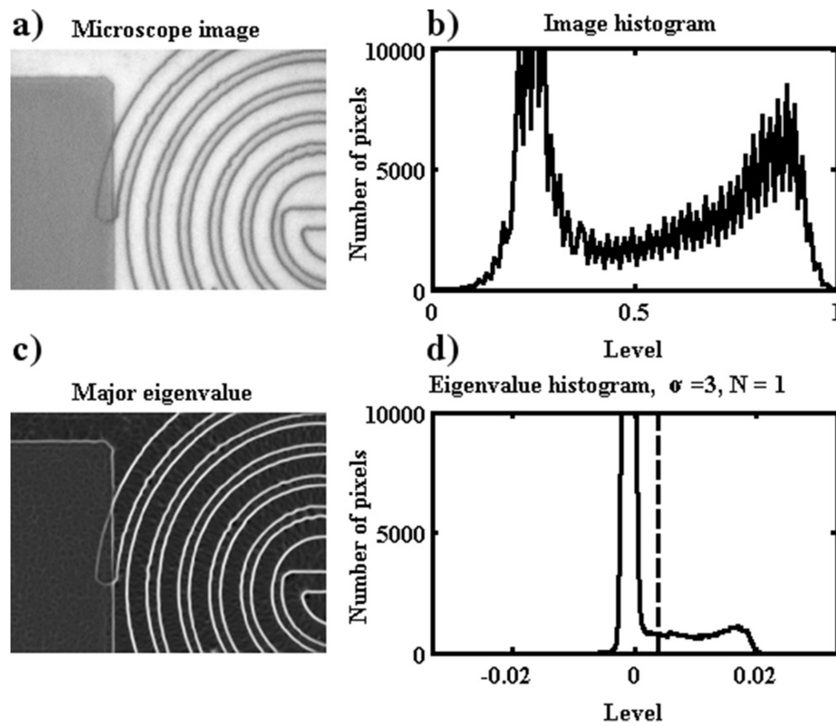

Figure 8. Image processing for HAR spring: (a) microscope image, (b) image intensity histogram, (c) spatial variation of major eigenvalue, and (d) histogram of eigenvalue showing Otsu threshold.

substrate areas. Valleys in brightness can be obtained from the second derivatives of B, namely $H_{yy} = \partial^2 B/\partial y^2$, $H_{zz} = \partial^2 B/\partial z^2$ and $H_{yz} = \partial^2 B/\partial y \partial z$ [35, 36]. The differentiation is carried out by convolution of B with matrix representations of discrete second order differential operators. The local results are then placed in a 2×2 matrix $[H_{yy}\ H_{yz}, H_{yz}, H_{zz}]$, whose eigenvalues are then found as:

$$\lambda_{1,2} = \frac{1}{2}\left\{H_{yy} + H_{zz} \pm \surd\left(H_{yy}^2 + H_{zz}^2 - 2H_{yy}H_{zz} + 4H_{yz}^2\right)\right\}. \quad (6)$$

The eigenvalues give the principal curvatures of B, and a valley in brightness corresponds to a high value of the major eigenvalue and a near-zero value of the minor eigenvalue. However, detection of the former may suffice. To reduce noise, differentiation should be carried out on a low-pass filtered image. Smoothing can be carried by convolution with the discrete representation of a Gaussian function [31]:

$$G(y, z) = \frac{1}{2\pi\sigma^2} \exp\left\{-\frac{\left(y^2 + z^2\right)}{2\sigma^2}\right\}. \quad (7)$$

The standard deviation σ should be chosen appropriately; too small a value will fail to reduce noise sufficiently, while too large a value will blur detail. Here we have used $\sigma = 3$. To improve speed, the differentiation is carried out on the Gaussian kernel itself rather than the image. Only one convolution is then required.

The levels separating the different classes must then be found. Many methods have been developed [37, 38], and one of the most useful is by Otsu [39]. The simplest version assumes two classes, and adjusts the threshold to ensure that intra-class variance is minimized and inter-class variance is maximized. Multi-level algorithms achieve the same with multiple thresholds [40]. Both are available in MATLAB.

The Otsu method works best if there are well-separated classes, of approximately equal size. Difficulties arise if there are overlapping classes, with one or more dominant. Figure 8(c) shows the spatial variation of the major eigenvalue, and figure 8(d) the corresponding histogram. The distribution is again bimodal, but the background now appears as a large peak with near-zero curvature, while the valley features appear as a broad satellite. The dashed line shows the threshold obtained using the single-level Otsu method. The green lines on figure 9(a) shows the features extracted by binarization about this level, superimposed on the original image. All NEMS features and MEMS edges have been extracted successfully. In fact, figure 9 shows similar results for all the structures in figure 2; in each case, feature extraction has succeeded using the same algorithm. However a $\times 1.6$ intermediate magnifier was used in figure 9(d) (which has the smallest feature spacing) to improve clarity.

We now consider whether NEMS features may be separated from the edges of MEMS features. Figures 10(a)–(d) shows the optical image, the image brightness histogram, the spatial variation of the major eigenvalue and the eigenvalue histogram obtained for the micro-gripper structure in figure 2(b). The brightness histogram is again bimodal, due to the difference in brightness of the largely uniform substrate and the MEMS-half of the grip. However, the eigenvalue distribution is clearly trimodal, since the MEMS edges appear slightly darker than NEMS features in the eigenvalue image. This suggests that the distribution may actually be partitioned into three classes using a two-level Otsu method, and the dashed lines show the thresholds thus obtained.

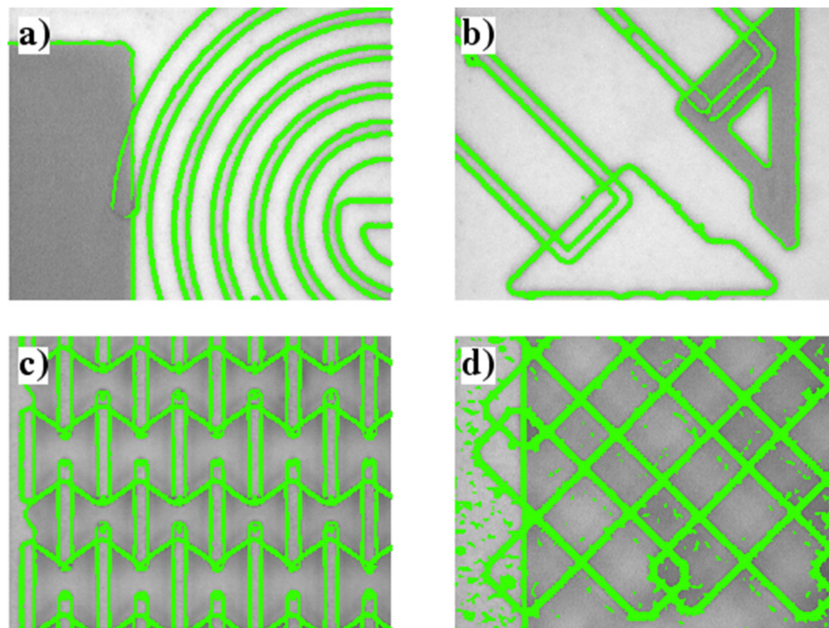

Figure 9. MEMS and NEMS line features extracted together from optical images of (a) spring, (b) gripper, (c) and (d) cellular materials.

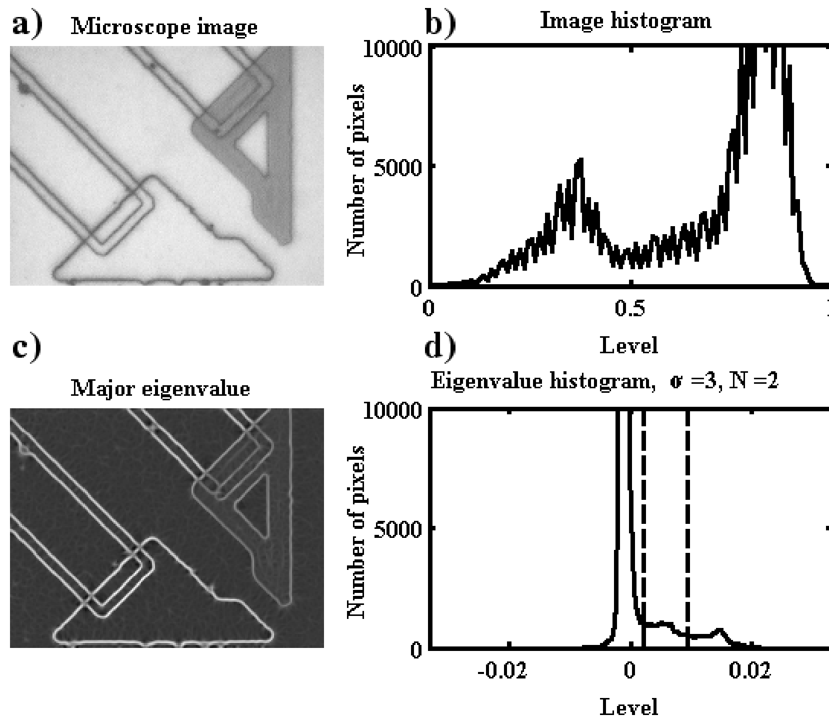

Figure 10. Image processing for HAR gripper: (a) microscope image, (b) histogram of image intensity, (c) spatial variation of major eigenvalue, and (d) histogram of eigenvalue, showing multiple Otsu thresholds.

Even with successful thresholding, multi-level separation is non-trivial. We illustrate the problem in figure 11 using a 1D example, which shows the spatial variation of the major eigenvalue derived from a line image containing two feature types and hence containing two different peak heights. Figure 11(a) shows how separation from background using a single threshold (dotted) yields both peaks together (in green), as before. Figure 11(b) shows separation of the higher peak alone (in blue), using a larger threshold. However, the attempt to separate peaks into two groups (in blue and red) using different thresholds in figure 11(c) fails, since the shoulders of the higher peak are grouped with the lower peak. Our solution is to exploit wide feature spacing and use a mask to exclude shoulders of the higher class from the lower class. The mask is constructed by convolving upper-level features with a top-hat function and binarizing the result, here yielding the cyan trace in figure 11(c) and the separation in figure 11(d).

For 2D variations, convolution with a $2M + 1 \times 2M + 1$ matrix of ones will broaden upper-level features by M pixels. Figures 12(a) and (b) shows separated MEMS and NEMS

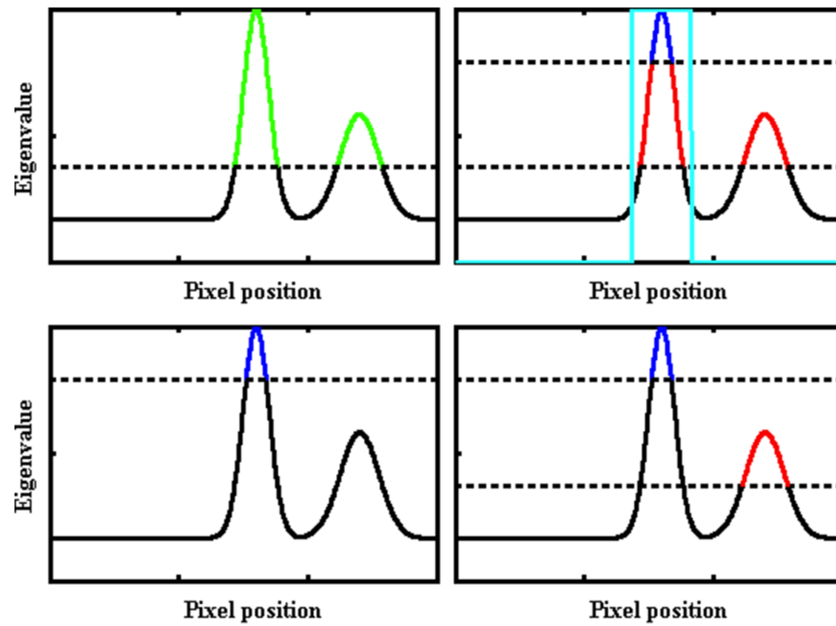

Figure 11. Illustrative 1D eigenvalue profile for NEMS and MEMS features, showing (a) single-value thresholding to extract all lines, (b) single-value thresholding to extract NEMS only, (c) double value thresholding and mask, and (d) double-value thresholding with masking to extract NEMS and MEMS separately.

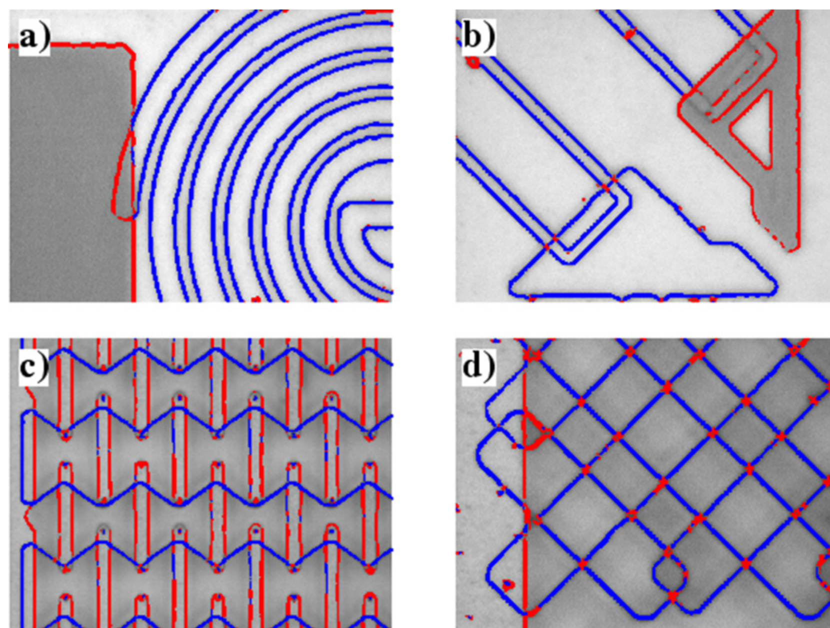

Figure 12. MEMS and NEMS line features extracted separately from optical images of (a) spring, (b) gripper and (c) and (d) cellular materials.

features (red and blue, respectively) for the two structures with residual resist, both obtained with $M = 2$ and a two-level Otsu scheme. With only two thresholds, legacy mesas cannot be separated from MEMS and NEMS, and have been assigned into the MEMS class. Separation was less satisfactory for the two structures without residual resist. Figures 12(c) and (d) therefore shows results obtained using the upper two thresholds of a three-level Otsu scheme. Legacy mesas have now been assigned into the NEMS class. In addition, separation has failed in figure 12(d) in two characteristic regions: intersections of nanoscale features, and regions containing closely spaced features. Brightness curvature must be inherently zero at the first location, and reduced by diffraction at the second. Further work is therefore needed to improve the specificity of the separation algorithm. Despite this, it is extremely encouraging that NEMS structures may not only be imaged optically but also analysed in this way.

5. Conclusions

We have demonstrated theoretically and experimentally that widely spaced, high-aspect ratio silicon NEMS are visible

under white-light illumination in a bright-field optical microscope, as dark lines on a light background. However, further work is clearly required to investigate the effects of diffraction from closely spaced features, additional surface coatings in typical device structures, and alternative modalities (for example, dark-field imaging). This characteristic allows nanoscale features and the edges of microscale features to be separated from background in optical images using valley detection. Non-linear processing then allows nanoscale parts to be separated from microscale parts, but further work is again required to reduce the content dependence of the segmentation algorithm. More accurate feature location may easily be achieved by skeletonisation, providing the basis of a simple NEMS metrology system and enabling measurement of static deflections for comparison with elastic theory. It is likely that the method could be extended to dynamic deflections using pulsed illumination and video processing.

Acknowledgments

The Authors are grateful to Dr M M Ahmad for assistance with device processing, and to an unnamed Referee for his suggestions to improve the manuscript.

ORCID iDs

R R A Syms https://orcid.org/0000-0003-0901-8314

References

[1] Craighead H G 2002 Nanoelectromechanical systems *Science* **390** 1532–5
[2] Ekinci K L and Roukes M L 2005 Nanoelectromechanical systems *Rev. Sci. Instrum.* **76** 061101
[3] Liu D and Syms R R A 2014 NEMS by sidewall transfer lithography *IEEE J. Microelectromech. Syst.* **23** 1366–73
[4] Liu D and Syms R R A 2015 NEMS by multilayer sidewall transfer lithography *28th IEEE MEMS. Conf. (Estoril, Portugal, 18–22 January)*
[5] Syms R R A, Liu D and Ahmad M M 2017 Nanostructured 2D cellular materials by sidewall transfer lithography NEMS *J. Micromech. Microeng.* **27** 075003
[6] Sohn Y-I, Burek M J, Kura V, Keams R and Loncar M 2015 Dynamic actuation of single-crystal diamond nanobeams *Appl. Phys. Lett.* **107** 243106
[7] Nyyssonen D and Larrabee R D 1991 Submicrometer linewidth resolution in the optical microscope *J. Res. Natl Bur. Stand.* **92** 187–204
[8] Creath K 1991 Submicron linewidth measurement using an interferometric optical profiler *Proc. SPIE* **1464** 474–83
[9] Morgan S P, Choi E, Somekh M G and See C W 2001 Interferometric optical microscopy of subwavelength grooves *Opt. Commun.* **187** 29–38
[10] Hopkins H H 1953 On the diffraction theory of optical images *Proc. R. Soc.* A **217** 408–32
[11] Kintner E C 1978 Method for the calculation of partially coherent imagery *Appl. Opt.* **17** 2747–53
[12] Nyyssonen D 1982 Theory of optical edge detection and imaging of thick layers *J. Opt. Soc. Am.* **72** 1425–36
[13] Nyyssonen D and Kirk C P 1988 Optical microscope imaging of lines patterned in thick layers with variable edge geometry: theory *J. Opt. Soc. Am.* A **5** 1270–80
[14] Sheridan J T and Sheppard C J R 1993 Coherent imaging of periodic thick fine isolated structures *J. Opt. Soc. Am.* A **10** 614–32
[15] Sheridan J T and Sheppard C J R 1994 Modelling of images of square-wave gratings and isolated edges using rigorous diffraction theory *Opt. Commun.* **105** 367–78
[16] Sheridan J T and Köurner T O 1995 Imaging periodic surface relief structures *J. Microsc.* **177** 95–107
[17] Tamir T, Wang H C and Oliner A A 1964 Wave propagation in sinusoidally stratified dielectric media *IEEE Trans. Microw. Theory Tech.* **MTT-12** 323–25
[18] Burkhardt C B 1966 Diffraction of a plane wave at a sinusoidally stratified dielectric grating *J. Opt. Soc. Am.* **56** 1502–609
[19] Chu R S and Kong J A 1977 Modal theory of spatially periodic media *IEEE Trans. Microw. Theory Tech.* **MTT-25** 18–24
[20] Moharam M G and Gaylord T K 1983 Three-dimensional vector coupled wave analysis of planar-grating diffraction *J. Opt. Soc. Am.* **73** 1105–12
[21] Moharam M G and Gaylord T K 1983 Rigorous coupled-wave analysis of grating diffraction—*E*-mode polarization and losses *J. Opt. Soc. Am.* **73** 451–5
[22] van Haver S, Braat J J M, Janssen A J E M, Janssen O T A and Pereira S F 2009 Vectorial aerial-image computations of three-dimensional objects based on the extended Nijboer–Zernike theory *J. Opt. Soc. Am.* A **26** 1221–34
[23] Capoglu R, Rogers J D, Taflove A and Backman V 2012 The microscope in a computer: image synthesis from three-dimensional full-vector solutions of Maxwell's equations at the nanometer scale *Prog. Opt.* **57** 1–91
[24] Prewitt J M S and Mendelsohn M L 1966 The analysis of cell images *Ann. New York Acad. Sci.* **128** 1035–53
[25] Price C A, Symonova O, Mileyko Y, Hilley T and Weitz J S 2011 Leaf extraction and analysis framework graphical user interface: segmenting and analyzing the structure of leaf veins and areoles *Plant Physiol.* **155** 236–45
[26] Frangi A F, Niessen W J, Vincken K L and Viergever M A 1998 Multiscale vessel enhancement filtering *Medical Image Computing and Computer-Assisted Intervention—MICCAI'98* (*Lecture Notes in Computer Science* vol 1496) ed W M Wells *et al* (Berlin: Springer)
[27] White J M and Rohrer G D 1983 Image thresholding for optical character recognition and other applications requiring character image recognition *IBM J. Res. Dev.* **27** 400–11
[28] Sherlock B G, Monro D M and Millard K 1992 Algorithm for enhancing fingerprint images *Electron. Lett.* **28** 1720–1
[29] Moganti M, Erkal F, Dagli C H and Tsunekawa S 1996 Automatic PCB inspection algorithms: a survey *Comput. Vis. Image Understand.* **63** 287–313
[30] Otwagin A and Doudkin A 2006 An MPI-based framework for parallel processing of integrated circuits layout images *Computing* **5** 55–61
[31] Babaud J, Witkin M, Baudin M and Duda R O 1986 Uniqueness of the Gaussian Kernel for scale-space filtering *IEEE Trans. Pattern Anal. Mach. Intell.* **PAMI-8** 26–33
[32] Davis L S 1975 A survey of edge detection techniques *Comput. Graph. Image Process.* **3** 248–70
[33] Sobel I and Feldman G 1968 A 3 × 3 isotropic gradient operator for image processing *Presented at the Stanford Artificial Intelligence Project*
[34] Canny J F 1986 A computational approach to edge detection *IEEE Trans. Pattern Anal. Mach. Intell.* **PAMI-8** 679–98

[35] Haralick R M 1983 Ridges and valleys on digital images *Comput. Vis. Graph. Image Process.* **22** 28–38
[36] Eberly D, Gardner R, Morse B, Pizer S and Scharlach C 1994 Ridges for image analysis *J. Math. Imaging Vis.* **4** 353–73
[37] Sahoo P K, Soltani S and Wong A K C 1988 A survey of thresholding techniques *Comput. Vis. Graph. Image Process.* **41** 233–60
[38] Sezgin M and Sankur B 2004 Survey over image thresholding techniques and quantitative performance evaluation *J. Electron. Imaging* **13** 146–65
[39] Otsu N 1979 A threshold selection method from gray-level histograms *IEEE Trans. Syst. Man Cybern.* **SMC-9** 62–6
[40] Liao P S, Chen T S and Chung P C 2001 A fast algorithm for multilevel thresholding *J. Inform. Sci. Eng.* **17** 713–27
[41] Saha P K, Borgefors G and de Baja G S 2016 A survey on skeletonization algorithms and their applications *Pattern Recognit. Lett.* **76** 3–12
[42] Bhardwaj J K and Ashraf H 1995 Advanced silicon etching using high density plasmas *Proc. SPIE* **2639** 224–33
[43] Benitez A, Esteve J and Bausells J 1995 Bulk silicon microelectromechanical devices fabricated from commercial bonded and etched-back silicon-on-insulator substrates *Sensors Actuators* **A50** 99–103
[44] Green M A and Keevers M J 1995 Optical properties of intrinsic silicon at 300 K *Prog. Photovolt., Res. Appl.* **3** 189–92
[45] Bücher K, Bruns J and Wagemann H G 1994 Absorption coefficient of silicon: an assessment of measurements and the simulation of temperature variation *J. Appl. Phys.* **75** 1127–32